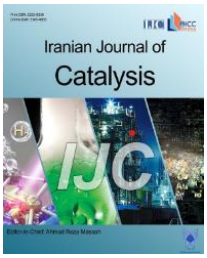

Iran. J. Catal., 2026; 16(1): 141-156

Iranian Journal of Catalysis (IJC)

https://doi.org/10.57647/ijc.2026.1601.09

Research Article

# Fabrication of g-$C_3N_4$/Cu-MOF/$Nd_2O_3$@NiO Nanocomposite for Dual Photocatalytic Applications: Methylene Blue Degradation and Hydrogen Peroxide Production

Rubab Islam[1], Noor Fatima Tariq Siddiqui[1], Muhammad Tariq[1,*], Khalid Mahmood[2], Ajaz Hussain[2], Shabbir Hussain[3], Muhammad Imran[4], Jafir Hussain Shirazi[5,*]

[1]*Division of Inorganic Chemistry, Institute of Chemical Sciences, Bahauddin Zakariya University, Multan, Pakistan*
[2] *Division of Organic Chemistry, Institute of Chemical Sciences, Bahauddin Zakariya University, Multan, Pakistan*
[3] *Institute of Chemistry, Khwaja Fareed University of Engineering and Information Technology, Rahim Yar Khan, Pakistan*
[4]*Institute of Chemistry, The Islamia University of Bahawalpur, Bahawalpur, Pakistan*
[5]*Department of Pharmaceutics, Faculty of Pharmacy, The Islamia University of Bahawalpur, Bahawalpur, Pakistan*
*
**Corresponding authors:**muhammadtariq@bzu.edu.pk, mtnazir@yahoo.com, jafirshirazi@gmail.com

**Article History:**

Received:
27 October 2025

Revised:
09 December 2025

Accepted:
16 December 2025

Published Online:
24 December 2025

Published in Issue:
31 March 2026

© 2026 The Author(s). Published by the OICC Press under the terms of the CC BY 4.0, Creative Commons Attribution License, which permits use, distribution and reproduction in any medium, provided the original work is properly cited.

**Abstract**

In the present report, a novel photocatalyst g-$C_3N_4$/Cu-MOF/$Nd_2O_3$@NiO was prepared using g-$C_3N_4$, Cu-MOF, and $Nd_2O_3$@NiO as the individual components using an ultrasonic-assisted wet-impregnation method. Fourier Transform Infrared (FTIR) spectroscopy, X-ray Diffraction (XRD), Scanning Electron Microscopy (SEM), and Energy Dispersive X-ray (EDX) analysis of the nanocomposite and its individual components were performed for vibrational, morphological, structural, and elemental characterization, respectively. The appearance of vibrational bands at 813 $cm^{-1}$ for g-$C_3N_4$, 665 $cm^{-1}$ for the Nd-O, 511 $cm^{-1}$ for NiO, and 599 $cm^{-1}$ for Cu-O indicates preparation of g-$C_3N_4$/Cu-BDC/$Nd_2O_3$@NiO nanocomposite. An irregular flake-like morphology of the nanocomposite was observed in SEM images. The appearance of sharp peaks in X-ray diffraction analysis indicated the crystalline nature of the nanocomposite and its individual components. EDX analysis indicated the presence of all elements that made up the composition of the nanocomposite and its individual components. A comprehensive photocatalytic study using nanocomposite and its individual components as photocatalysts was conducted on the degradation of Methylene blue (MB) as a target pollutant. The results indicated that the nanocomposite degraded the target pollutant more efficiently than its individual components at various parameters such as pH, time, concentration of catalyst, and pollutant. The nanocomposite showed maximum degradation of 91% at pH 11, a catalyst dose of 10 mg, and 140 minutes of irradiation time in sunlight. The nanocomposite and its individual components were also tested for the production of Hydrogen Peroxide ($H_2O_2$), and a higher production rate of 0.19 mg/L was obtained by the nanocomposite.

**Keywords:** Hydrogen Peroxide; Graphitic Carbon Nitride; Multicomponent Photocatalyst; Methylene blue; Neodymium Oxide; Photocatalytic Degradation

**Cite this article:** R., Islam, N., Fatima Tariq Siddiqui, M., Tariq, Kh., Mahmood, A., Hussain, Sh., Hussain, M., Imran, J. Hussain Sherazi, Iran. J. Catal. **16** (2026) 141-156. https://doi.org/10.57647/ijc.2026.1601.09

## 1. Introduction

Heavy industrialization increases contamination of the water, air, and land because growing populations raise demand for industrial goods. Additionally, the absence of efficient industrial discharge treatment techniques in emerging nations is a worldwide problem for both people and the environment [1]. Currently, water preservation and purification, as well as their environmental ramifications, are critical challenges for human survival across the world. Water pollution has lately arisen as a serious worldwide problem, becoming a main topic of scientific investigation [2]. Pollution, urbanization, industrial activity, and climate change all worsen water scarcity [3]. Water shortage is caused by contamination from a variety of leftover items, counting pesticides, medications, dyes, antibiotics, organic and inorganic contaminants such as metals, micro pollutants, and a wide range of inorganic compounds. Uncontrolled flow into water bodies from a variety of industrial operations, hospitals, and wastewater sources is frequently associated with water contamination [4]. Dyes serve as essential components in a wide array of commercial industries, including textiles, clothing, cosmetics, food, beverages, and pharmaceuticals [5].

Furthermore, as the textile industry grows, there are growing concerns about environmental pollution caused by dyes, which, because of their toxic and long-lasting nature, significantly affect the environment. These organic chemicals are poisonous, non-biodegradable, resistant to decomposition, and can remain in the environment [6]. Dyes must now be thoroughly removed before being released into bodies of water. Because of their high chemical stability, most organic dyes remain in flowing water for longer periods of time, slowing photosynthesis, hindering the growth of marine organisms by obstructing sunlight and using oxygen, and lowering the value of streams. Decomposing dye impurities into non-toxic compounds is tough. Due to slower biodegradation and extremely hazardous nature, the breakdown of dyes in textile wastewater has garnered significant research.

Dyes like Methylene blue (MB), a cationic dye, have been employed as a colorant in several industries [4]. Methylene blue (MB) dye contamination is widely disseminated because of its use in the dying and printing cloth industries [7]. The azo functional group (-N=N-) that is in the MB structure is regarded as carcinogenic [8]. Moreover, MB breathing influences digestive system aches, respiratory system illness, and nervous system diseases. Furthermore, being toxic to aquatic and other creatures, MB can cause numerous diseases in humans, such as abdominal pain, nausea, headaches, vision damage, dizziness, and anemia. It also has negative impacts on aquatic life and other organisms. There are many methods for eradicating impurities from polluted water, including precipitation, coagulation, filtration, adsorption, and oxidation [9].

The most popular method among them for eliminating contaminants from water, aquatic environments, and effluents is adsorption. Several adsorbents have been examined for the breakdown of dyes; however, the use of huge quantities of adsorbents has the drawback of being costly and non-biodegradable [10]. Additionally, a considerable quantity of secondary pollutants may be produced by these actions. However, the economic feasibility of most of these outdated techniques is in doubt due to their high catalyst requirements. Consequently, a number of research institutions are working to resolve this crucial problem in the long run [11]. Advanced oxidation process appears to be the most suitable method to remove pollutants as it is an environmentally friendly and inexpensive process [12].

Among the novel oxidation techniques or advanced oxidation processes (AOP), heterogeneous photo-catalysis appears as a growing destructive technology, leading to the complete mineralization of the majority of organic contaminants. AOPs are defined as processes that depend on in-situ creation of highly oxidizing radicals, chiefly hydroxyl ($^{\bullet}OH$) and superoxide radicals ($O_2^{\bullet-}$), to transform dangerous organic contaminants into less toxic ones. Semiconductor-mediated heterogeneous photocatalysis is a potential approach for energy and environmental applications in AOPs. Because of its advantages, such as affordability, non-toxicity, and full mineralization, it has grown into a fast-developing subject of study during the last few decades [13].

Metal organic frameworks (MOFs) MOFs have become an innovative class of porous materials with significant photocatalytic, sensor, detection of pollutants, and storage applications [14, 15]. Metal ions and organic ligands are combined in three-dimensional areas to generate MOFs. Over the past decades, MOFs have drawn a lot of attention due to their unique properties, which include high porosity, low density, thermal stability, vast surface area, chemical functionalities that can be adjusted, and the ability to harvest light. MOFs are attracting a lot of scientific interest because of their capacity to absorb visible light [16, 17].

Because of their high surface area and ability to be produced using commercially accessible chemicals, copper-based MOFs stand out among the others. Because of its wealth of resources, affordability, non-hazardous qualities, and most significantly, complexation strength, copper (Cu), a classical transition metal, was chosen as one of the most desirable metals to employ in the creation of MOFs.

The interaction between Cu(II) from the metal and -O- from the organic ligand is responsible for the high and exceptional stability of Cu-based MOFs. Terephthalic

10.57647/ijc.2026.1601.09

acid is a typical ligand that is readily available and has relatively low toxicity [18].

Terephthalic acid can be obtained from waste polyethylene terephthalate (PET) bottles. PET can be used to build metal-organic frameworks (MOFs) because it contains up to 85 wt. % terephthalic acid ($H_2BDC$), which is ideal for organic linkers in MOF structures [19]. Wastes plastic PET bottles have been used in many industries and in daily life as packaging materials due to their high resistance to moisture, sunlight, and microorganisms, as well as their high transparency, design flexibility, inertness towards food, and affordability. PET bottles are one of the most prevalent waste materials on the planet due to their enormous usage.

In fact, the anticipated annual global consumption of PET is about 24 million tons, and it is rising steadily. Because PET is not biodegradable, this leads to major environmental problems. The use of non-eco-friendly materials, such as waste, to create environmentally friendly products that can subsequently be used again for environmental treatment is an alternative to the currently popular methods of getting rid of PET waste. In metal-organic frameworks (MOFs), organic linkers create a charge-separated state by absorbing photons. Nevertheless, photocatalytic activity is hampered by the recombination of the excited electron holes. Therefore, pairing MOF with an appropriate semiconductor such as graphite carbon nitride, metal oxides, etc, increases its photocatalytic activity while decreasing charge carrier recombination rates [20]. g-$C_3N_4$ is mostly made up of the earth's abundant elements C and N.

It offers a cost-effective and non-hazardous, making it a suitable material for environmental protection. The g-$C_3N_4$ has the advantages of stability and responsiveness to visible light. Therefore, it finds wide-ranging use in the photocatalytic destruction of organic contaminants [21]. Graphitic carbon nitride (g-$C_3N_4$) is a metal-free material that has sparked considerable interest in the field of water pollution removal due to its exceptional qualities, such as non-toxicity, low cost, ease of synthesis, good stability, and visible-light absorption band-gap (2.73 eV).

The practical uses of g-$C_3N_4$ have been restricted by two major factors: fast electron-hole recombination and low surface area. These disadvantages can be solved using material design tactics such as morphological control, doping, and, especially *via* the production of nanocomposites [22], e.g., g-$C_3N_4$ [23], g-$C_3N_4$/$Bi_2O_3$/$TiO_2$ [24], $Ag_3PO_4$/Zr-BDC/g-$C_3N_4$ [25] have been used for the photocatalytic degradation of MB dye. The advancement of technological innovations in fabricating metal oxide nanoparticles has facilitated the development of diverse photocatalysts. Combining metal oxides with MOFs in composites enhances surface area, catalytic activity, and stability, offering superior photocatalytic performance. $SnO_2$/MOF-5 was used as a photocatalyst for the degradation of eriochrome black T (EBT) and showed an excellent photocatalytic activity because $SnO_2$ promoted better $e^-/h^+$ pair separation [26]. The semiconductor photocatalysts, such as $NiFe_2O_4$ and $ZnFe_2O_4$ ferrites, were applied for efficient degradation of the drug metronidazole [27, 28].

The $SnO_2$-$BiVO_4$-CuO catalyst degraded phenazopyridine more compared to its individual components SnO2, BiVO4, and CuO [29]. In comparison to the frequently used semiconductor materials, research have been conducted on inner transition metal oxides. Neodymium oxide ($Nd_2O_3$) offers excellent light absorption capacity [30]. $Nd_2O_3$ can be used as a catalytic material that showed an excellent prospective for photocatalytic degradation [31]. Nickel oxide has emerged as a focus point in nanotechnology owing to its remarkable electrical and optical features.

NiO, a transition metal oxide, have several uses, especially in fields like energy storage, sensors, and catalysis. One important characteristic that increases its efficacy in a number of photocatalytic activities, including the breakdown of organic contaminants, is its capacity to absorb light and promote charge carrier generation [32, 33]. Nickel oxide nanoparticles (NiO-NPs) that can cause electron excitation through irradiation while simultaneously destroying a wide range of pollutants [34, 35]. Establishing a link with a suitable band structure by mingling with others can efficiently raise the range of sunlight absorption and haste the rate at which electron–hole pairs are isolated [36].

As a result, the grouping of $Nd_2O_3$ to NiO was made to enhance the photocatalytic application against MB by separating $e^-/h^+$ pair, prompting kinetics of charge transfer between the metal oxides, and restricting recombination by increasing the lifetime of charge carriers. Moreover, the g-$C_3N_4$ array provides better charge carrier mobility, aids in avoiding photo-corrosion of MO [13].

Nano-composite was also used for the production of $H_2O_2$. Fuel cells, wastewater treatment, the chemical sector, and the medical field are just a few of the industries that use $H_2O_2$, a very significant green and adaptable oxidant. Because of its ease of storage and ability to replace fossil fuels, it has drawn a lot of attention as a liquid fuel [37].

As a powerful and environmentally friendly oxidant, hydrogen peroxide ($H_2O_2$) has the greatest active oxygen content (47.1 wt%). Water and oxygen are the only byproducts of hydrogen peroxide production. With these qualities, $H_2O_2$ plays a dynamic role in numerous areas, including organic synthesis, paper bleaching, wastewater treatment, disinfection, mining, and metal processing. As a consequence, $H_2O_2$ has been mentioned as one of the 100 most vital compounds [38]. It is assessed that the worldwide demand for $H_2O_2$ will reach 5.7 million tons by 2027 [39]. In the present study, a novel nanocomposite g-

$C_3N_4$-based Cu-MOF/$Nd_2O_3$@NiO was prepared by the combination of g-$C_3N_4$, Cu-BDC, $Nd_2O_3$@NiO, using an ultra-sonic assisted wet impregnation technique. The nanocomposite and its individual components were completely characterized using various analytical tools and used as a photocatalyst in the degradation of MB as a target pollutant and production of hydrogen peroxide. The optimization of various operating parameters, including the effect of pH and dose of photocatalyst, was achieved in MB photocatalytic degradation.

Scavengers' experiment ($AgNO_3$, EDTA-Na, ASC, and DMSO) was also performed for the determination of the species responsible for the degradation of the MB dye. The nanocomposite and its individual components were also tested as a catalyst for the production of hydrogen peroxide. The results indicated that more production of hydrogen peroxide was obtained by the nanocomposite than its individual components.

## 2. Experimental

### 2.1. Materials

Melamine (99% purity by DAEJUNG), terephthalic acid synthesized from PET bottles, copper nitrate tri-hydrate (99% purity by DAEJUNG), NaOH (98% purity by Icon Chemical), Hydrochloric acid (37% purity by Merck), Methylene Blue Dye (99% purity), DMF (≥99% by Merck), DCM, Neodymium nitrate hexa-hydrate (Sigma-Aldrich), Ethanol (95% purity by Sigma Aldrich), Thio-urea (98.5% purity by Riedel-deHaën), De-ionized water (99% purity) were used in the present research project.

### 2.2. Procedures for preparation of individual components and composite

#### 2.2.1. *Formation of g-$C_3N_4$*

g-$C_3N_4$ was prepared by utilizing the reported technique[13]. In short, 4.0 g of melamine was placed in a furnace for 4 hours at 500 °C. The calcined product, having a yellow color shown in Figure 1, was obtained after cooling.

#### 2.2.2. *Formation of benzene 1,4-dicarboxylic acid from waste PET bottles*

Benzene 1,4-dicarboxylic acid (BDC) was prepared from PET (polyethylene terephthalate) bottles by the reported process through the alkaline hydrolysis of PET Bottles [17]. 3:1 molar solution (mNaOH:mPET) containing sodium hydroxide and PET fragments was made and placed in a flask, with continuously heated to obtain a milky liquid. Then, filtration was done and concentrated hydrochloric acid was added to the filtrate to attain pH = 2, which results in the production of a white-colored solid. Then obtained $H_2BDC$ was washed with water several times and dried.

#### 2.2.3. *Formation of Cu-MOF using benzene 1,4-dicarboxylic acid*

Cu-MOF was prepared using benzene 1,4-dicarboxylic acid as an organic linker by the reported hydrothermal technique [17]. Benzene 1,4-dicarboxylic acid (0.9 g) and $Cu(NO_3)_2.3H_2O$ (1.2 g) were taken and dispersed in 90 mL DMF. The solution was placed in an autoclave at 100 °C for 24 hours, resulting in the formation of a blue product. The autoclave was cooled down, and the resulting product obtained after filtration was washed with DMF and DCM.

#### 2.2.4. *Formation of $Nd_2O_3$@NiO*

$Nd_2O_3$@NiO was synthesized by the reported method [40]. $Nd(NO_3)_3.6H_2O$ (0.1 M) and $Ni(OOCCH_3)_2.4H_2O$ (0.1 M) solutions of both were prepared in deionized water. Both solutions were mixed 0.2 M thiourea solution. The entire solution was put on a hot plate at 80 °C with continuous stirring.

During heating, 2.0 M NaOH was added to the above solution till the pH reached to 10. The beaker was placed aside to allow the precipitates to settle. Washing was done with a mixture of water and ethanol. Precipitates were dried at 80° C for 3 days. The obtained product was calcined at 600 °C for 6 hours.

#### 2.2.5. *Formation of composite g-$C_3N_4$ based Cu-BDC/$Nd_2O_3$@NiO*

The g-$C_3N_4$ based Cu-BDC/$Nd_2O_3$@NiO composite was fabricated using freshly prepared individual components by the ultra-sonic assisted wet-impregnation method. A 50 mL solution of ethanol/water in a 1:1 molar ratio was made. The individual components, g-$C_3N_4$, Cu-BDC, and $Nd_2O_3$@NiO, were taken in a 1:1:1 molar ratio. 0.1 g of g-$C_3N_4$ was added to an ethanol-water solution and ultra-sonicated for1 hour. After this, 0.09 g of Cu-BDC and 0.2 g of $Nd_2O_3$@NiO were added to the above solution and stirred for 24 hours. Then, the nanocomposite was centrifuged and dried at 70 °C in an oven.

The color of all synthesized individual components/precursors/pristine materials and final composite and schematic presentation of composite synthesis are presented in Figure 1 (A and B), respectively.

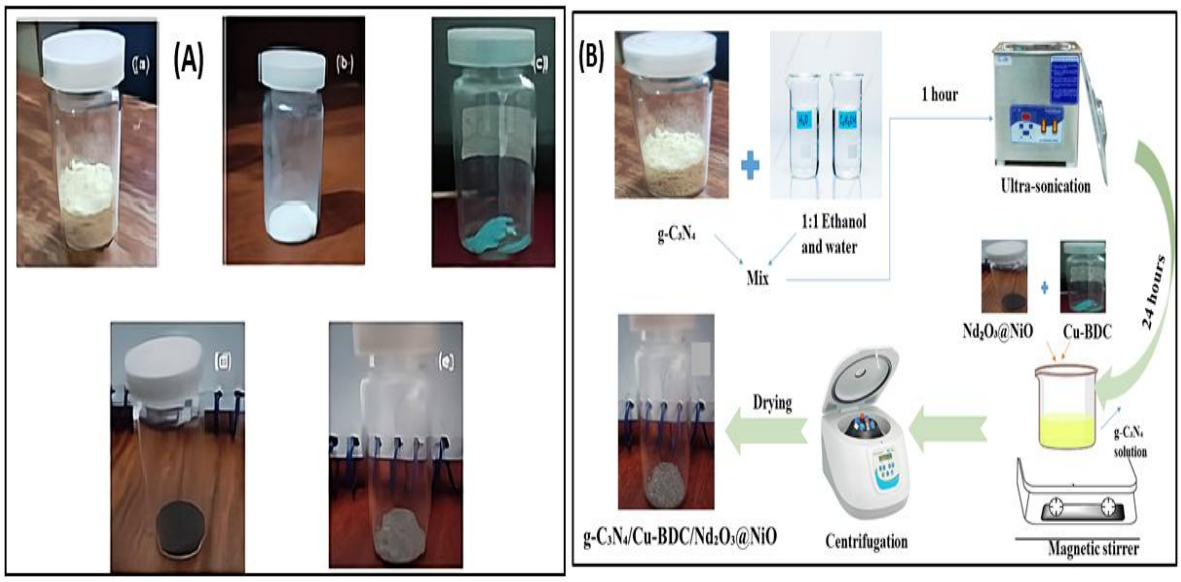


**Figure 1.** (A) Graphitic carbon nitride(a), Benzene 1, 4-dicarboxylic acid ($H_2BDC$) (b), Cu-MOF(c), $Nd_2O_3$@NiO(d), g-$C_3N_4$ based Cu-BDC/$Nd_2O_3$@NiO(e), and (B) Schematic Illustration for the preparation of the composite

### 2.3. Photocatalytic degradation procedure

The effective photocatalytic potential of the composite was evaluated by analyzing the photocatalytic degradation of dye methylene blue (MB). The target pollutant, methylene blue (10 mg/L), was first dissolved in water to make a stock solution of 100 mL. 5 mL solution was removed as a blank.

Then, the catalyst was added to the above solution. Before being exposed to light, the solution was stirred and kept in a dark environment for 30 minutes to reach equilibrium (adsorption-desorption). 5 mL was removed from the solution, and the remaining 90 mL solution was exposed to sunlight with stirring. After every 30 minutes of interval, 5 mL was collected from the solution to assess contaminant degradation percentage.

All photocatalytic degradation experiments were conducted outdoors during the months of June-July under direct sunlight in Multan city (Latitude: 30.18°, Longitude: 71.49°) between 11:00 AM and 2:00 PM, a time period during which solar intensity remains relatively stable and highest, with an average solar irradiance of 820–900 W/m².

The photocatalytic experimental setup picture is given in the supplementary file as Figure S1. The maximum absorption peak for methylene blue was attained at 663 nm in spectrophotometric analysis, which was used to assess percentage degradation. A photo-degradation experiment was performed using various range of photocatalyst doses (5-20 mg) and pH range (3-11) as reported earlier [41]. Percentage degradation was determined by the following equation.

$$\% \text{ Degradation} = [(C_o - Ct)/C_o] \times 100 \quad (1)$$

Here, $C_o$ shows primary concentration, whereas $C_t$ shows concentration taken with time.

### 2.4. Photocatalytic $H_2O_2$ production procedure

The photocatalytic production experiment of hydrogen peroxide was performed using an earlier reported procedure [37]. Briefly, the composite (20 mg) was dissolved in deionized water, and the obtained solution was stirred in the dark for 30 min to obtain an adsorption-desorption equilibrium.

The photocatalytic production of $H_2O_2$ was investigated under a visible light source (300 W tungsten bulb) in ambient air. After some time, a certain amount of the solution was taken, and containing the photo-catalyst was separated. $H_2O_2$ concentration was determined by a UV-1800 spectrophotometer at 350 nm based on the iodometric method [37].

In this method, the above solution was mixed with an equal volume of potassium iodide solution (0.4 M) and potassium hydrogen phosphate solution (0.1 M). The solution was left in the dark for 30 minutes, and the $H_2O_2$ concentration was determined by a UV-Vis spectrophotometer [42].

### 2.5. Analytical tools used for characterization

The g-$C_3N_4$ based Cu-BDC/$Nd_2O_3$@NiO composite and its individual components were characterized by a number of analytical techniques. FTIR Spectrophotometer (model Shimadzu 8400) was utilized in the wavenumber range of 4000-400 $cm^{-1}$ at room temperature. Cu tube (λ=1.5418 Å) was used to determine the nature of the synthesized materials using PXRD (Powder X-ray diffractometer MeasSrv (2Z5VTB2)) in the 10-80° range. SEM (scanning electron microscopy) FEI Nova 450 Nano SEM was used to determine the surface morphology of the prepared materials, while EDX was performed to evaluate elemental composition. A Shimadzu 1800 UV-visible

10.57647/ijc.2026.1601.09

spectrophotometer was used to record absorption spectra.

## 3. Results & discussion section

### 3.1. Infrared Spectroscopic Analysis

The infrared spectroscopic spectra were recorded in the range 4000-400 $cm^{-1}$ for stretching and bending vibrational analysis of the prepared g-$C_3N_4$ based Cu-BDC/$Nd_2O_3$@NiO composite and its individual components. The significant peaks related to M-O are illustrated in the fingerprint region ranging from (700-500 $cm^{-1}$) [43]. A peak perceived at 817 $cm^{-1}$ indicates triazine units of g-$C_3N_4$. Moreover, the bands at 1249 $cm^{-1}$ and 1437 $cm^{-1}$ are because of aromatic C-N stretching. Because of the atmospheric $CO_2$, the impurity peak can be viewed at 2345 $cm^{-1}$ [13].

All these relevant absorption bands have been compared with previously reported g-$C_3N_4$ [44, 45]. A peak observed at 3450 $cm^{-1}$ indicates the existence of the O-H stretching vibration in BDC. At 1720 $cm^{-1}$, there is an absorption band which illustrates C=O stretching. Band at 1575 $cm^{-1}$ illustrates the presence of aromatic C=C stretching vibration.

While the peak at 1442 $cm^{-1}$ illustrates symmetrical stretching vibration of $COO^-$ . Moreover, in MOF, the band at 1689 $cm^{-1}$ represents the C=O stretching. A sharp peak at 581 $cm^{-1}$ shows the existence of Cu-O bond. The presence of C=O, aromatic C=C, $COO^-$ and Cu-O band indicate the formation of Cu-BDC MOF and these results are comparable to previously reports[46]. The band at 678 $cm^{-1}$ refers to Nd-O stretching band. The presence of band at 515 $cm^{-1}$ indicates Ni-O stretching band. These relevant bands of Nd-O and Ni-O are comparable with previous reports [47, 48]. The presence of bands at 813 $cm^{-1}$ is because of bending vibration of triazine units, 665 $cm^{-1}$ for the Nd-O stretching, 511 $cm^{-1}$ for NiO stretching and 599 $cm^{-1}$ for Cu-O indicates successful formation of g-$C_3N_4$ based Cu-BDC/$Nd_2O_3$@NiO composite (as shown in Figure 2).

### 3.2. Electron microscopic analysis-SEM

The g-$C_3N_4$ based Cu-BDC/$Nd_2O_3$@NiO composite and its individual components were analyzed for determination of shape or morphology of prepared nanostructure. The results or images are shown in Figure 3. Figure 3 (a, b, c) shows the SEM images of Cu-BDC at different resolutions (1 µm, 4 µm and 10 µm) exhibiting irregular shaped porous morphology with agglomeration. The result is comparable with previous report [46]. SEM image of $Nd_2O_3$@NiO in Figure 3 (d, e, f) illustrates the irregular grains like morphology at different resolutions (1 µm, 4 µm and 10 µm). Figure 3 (g, h, i) at different resolutions (1 µm, 4 µm and 10 µm) shows images of g-$C_3N_4$ based Cu-BDC/$Nd_2O_3$@NiO exhibiting irregular flake like morphology with agglomeration.

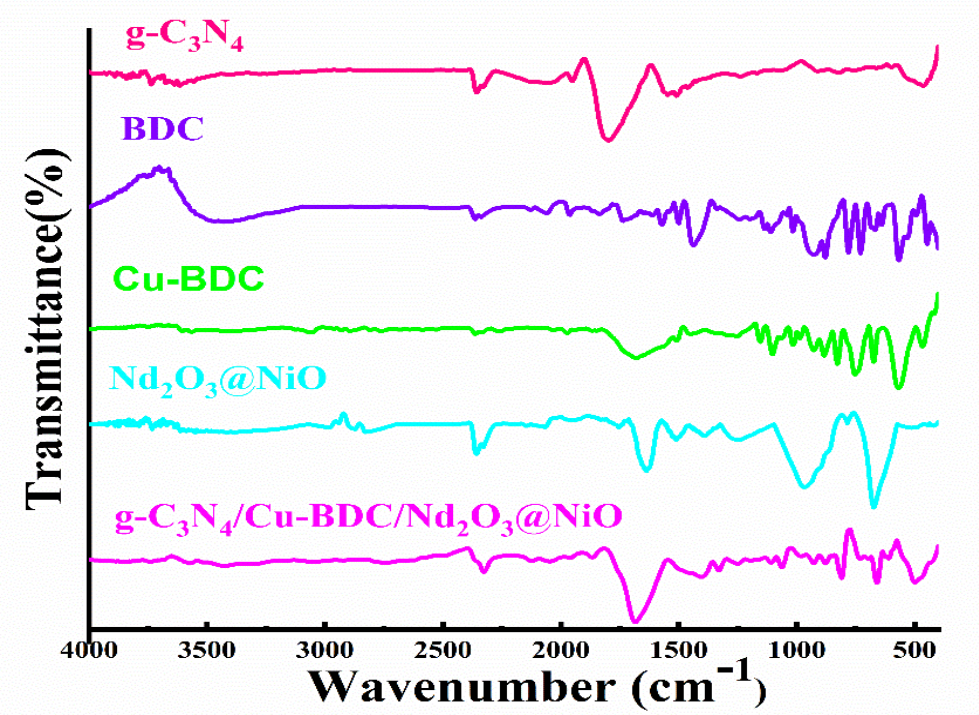


**Figure 2.** FTIR spectra (from top to bottom), graphitic carbon nitride(g-$C_3N_4$), Benzene 1,4-dicarboxylic acid (BDC), Cu-BDC MOF, $Nd_2O_3$@NiO, g-$C_3N_4$ based Cu-BDC/$Nd_2O_3$@NiO composite

10.57647/ijc.2026.1601.09

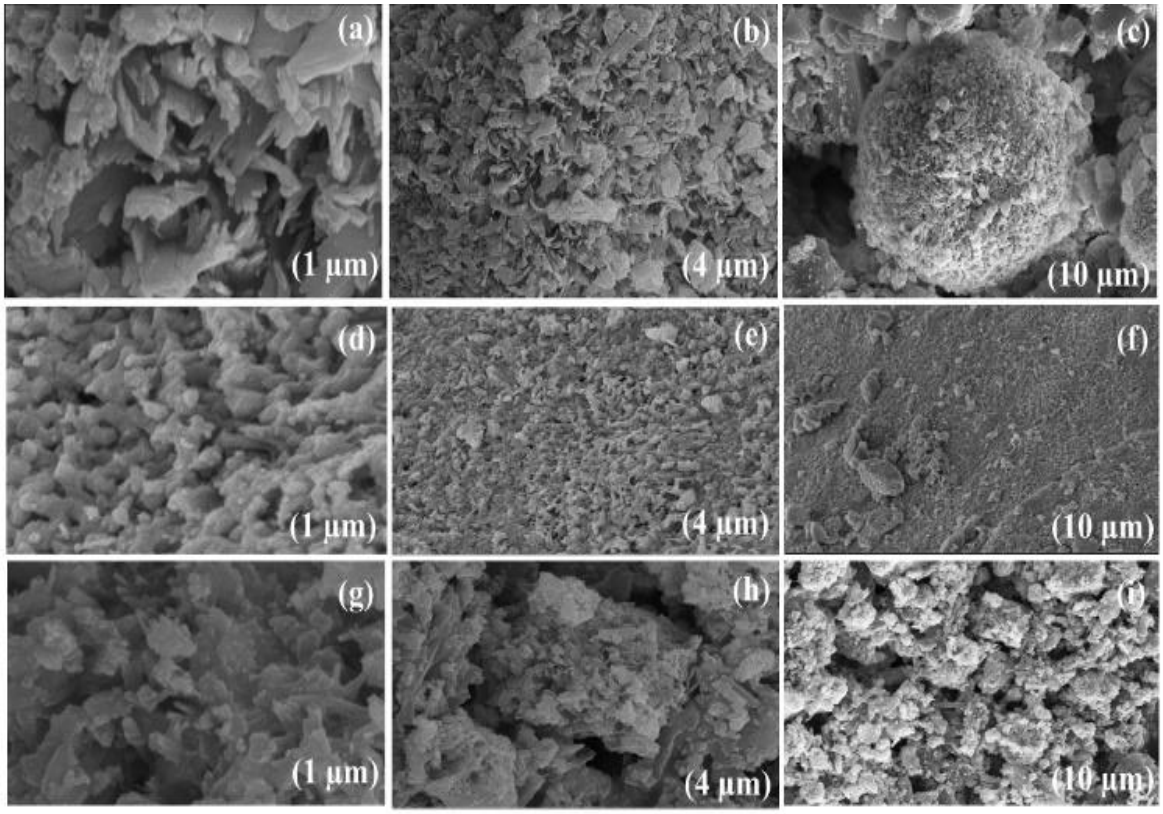


**Figure 3.** SEM images of Cu-BDC MOF (a, b, c), $Nd_2O_3$@NiO (d, e, f), g-$C_3N_4$ based Cu-BDC/$Nd_2O_3$@NiO composite (g, h, i)

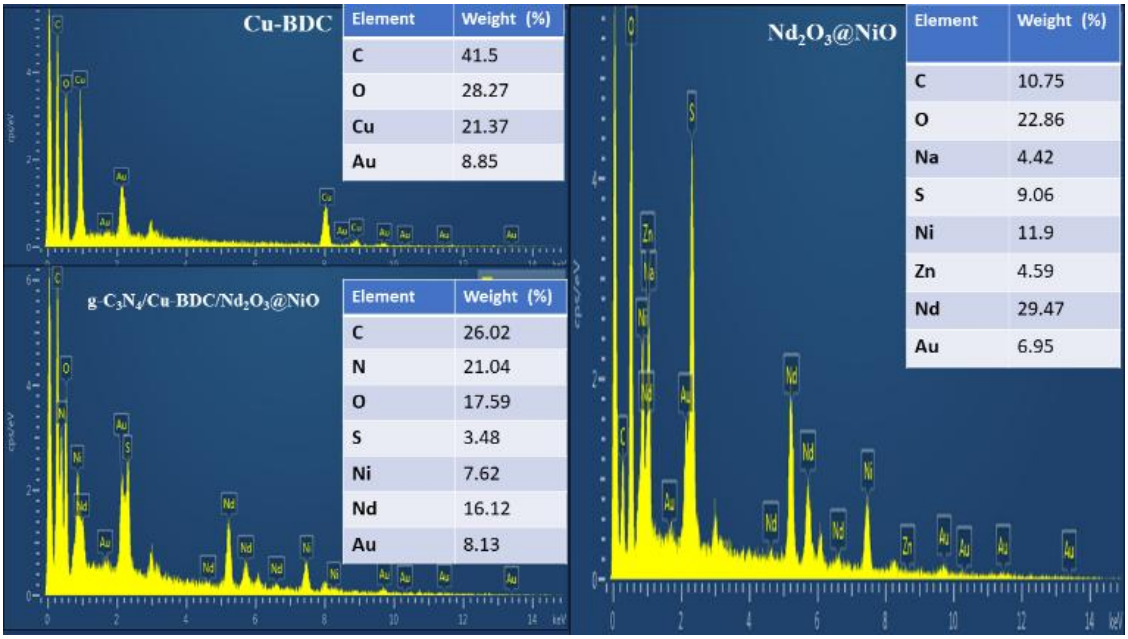


**Figure 4.** EDX analysis of Cu-MOF, $Nd_2O_3$@NiO, and g-$C_3N_4$ based Cu-BDC/$Nd_2O_3$@NiO composite

### 3.3. Elemental analysis

The elemental composition can be determined using energy dispersive X-ray (EDX) analysis of synthesized materials. Elemental spectra with weight % composition of g-$C_3N_4$ based Cu-BDC/$Nd_2O_3$@NiO composite and its individual components (Cu-BDC MOF and $Nd_2O_3$@NiO) are shown in Figure 4. EDX spectrum of Cu-BDC exposed the existence of 41.5 % of carbon, 28.27 % of oxygen, 21.37 % of copper, and 8.85 % of gold. EDX analysis of $Nd_2O_3$@NiO revealed the presence 10.75 % of carbon, 22.86 % of oxygen, 4.42 % of sodium, 9.06 % of sulphur, 11.9 % of nickel, 4.59 % of zinc, 29.47 % of neodymium and 6.95 % of gold. EDX spectrum of composite g-$C_3N_4$/Cu-BDC/$Nd_2O_3$@NiO showed the existence of 26.02 % of carbon, 21.04% of nitrogen, 17.59 % of oxygen, 3.48 % of sulphur, 7.62 % of nickel, 16.12 % of neodymium, and 8.13 % gold, with the exception of Cu, which might be due to its lesser amount. In the spectrum, a peak for Na is present due to NaOH as used

10.57647/ijc.2026.1601.09

in the metal oxide formation [12]. Similarly, peaks for S and C might be due to the use of thiourea during synthesis. The presence of Au in the spectrum might be due to gold coating. Zn might be due to contamination in the sample chamber.

### 3.4. Structural Analysis

The g-$C_3N_4$ based Cu-BDC/$Nd_2O_3$@NiO composite and its individual components (Cu-BDC MOF and $Nd_2O_3$@NiO) were analyzed by PXRD to confer their crystalline nature. The results in the form of XRD patterns are represented in Figure 5. The Figure 5(a) shows the XRD pattern of Cu-BDC MOF, having sharp peaks which indicate the crystalline nature of Cu-BDC MOF. Cu-BDC exhibited the major diffraction peaks at 9.7° (110), 16.59° (021), and 24.16° (131). This diffraction pattern has been compared with the previously reported diffractogram by Sutapa et al. [49] and found well match with it. Scherrer's formula was used to calculate the average crystallite size, indicated as:

$$D = K\lambda/\beta cos\theta \quad (2)$$

representing K as constant for Cu grid (0.94), λ is wavelength (1.5406 A°), β represents the FWMH (Full Width at half maxima), and θ illustrates the diffraction angle. The determined average crystallite size of Cu-BDC MOF is 15.16 nm according to the Scherrer formula. $Nd_2O_3$@NiO exhibited the diffraction peaks in Figure 5 (b) at 36.43° (111), 42.82° (200), 62.50° (220), 75.10° (311), and 79.06° (222) for NiO using JCPDS card no. 04-0835. While the peaks at 28.86° (100), 29.88° (002), 33.04° (101), 40.29° (102), 48.38° (110), 50.85° (103), 56.08° (201), 66.52° (202), 68.07° (104), 77.33° (211) were observed for $Nd_2O_3$.

These diffraction patterns of NiO and $Nd_2O_3$ were compared with JCPDS no. 04-0835 and JCPDS no. 41-1089, respectively, and with the previously reported pattern by Rahman et al., [40]. Sharp diffraction peaks show its better crystallinity. The average crystallite size was determined as 12.13 nm by Scherrer's formula. In the XRD pattern of g-$C_3N_4$ based Cu-BDC/$Nd_2O_3$@NiO composite (Figure 5 c), the presence of g-$C_3N_4$ is indicated by the peak that appeared at 27.78° [13]. The presence of Cu-BDC MOF is indicated by the important peaks present at 12.14°, 16.30°, and 22.38°. The distinct diffraction peak of Cu-BDC at 9.7° has been shifted to a higher angle at 12.14°, which may be ascribed to the incorporation of components in composite formation. The presence of NiO is indicated by the peaks present at 34.98°, 46.15°, 62.50°, 75.11°, and 79.11°. The presence of $Nd_2O_3$ is indicated by the peaks appeared at 28.98°, 29.90°, 33.85°, 40.45°, 46.15°, 50.86°, 56.56°, 66.55°, 69.56° and 77.11°.

The observed distinct diffraction peaks of $Nd_2O_3$ and NiO indicate the formation of a composite [40]. The average crystallite size of g-$C_3N_4$ based Cu-BDC/$Nd_2O_3$@NiO composite was determined as 14.08 nm by Scherrer's formula.

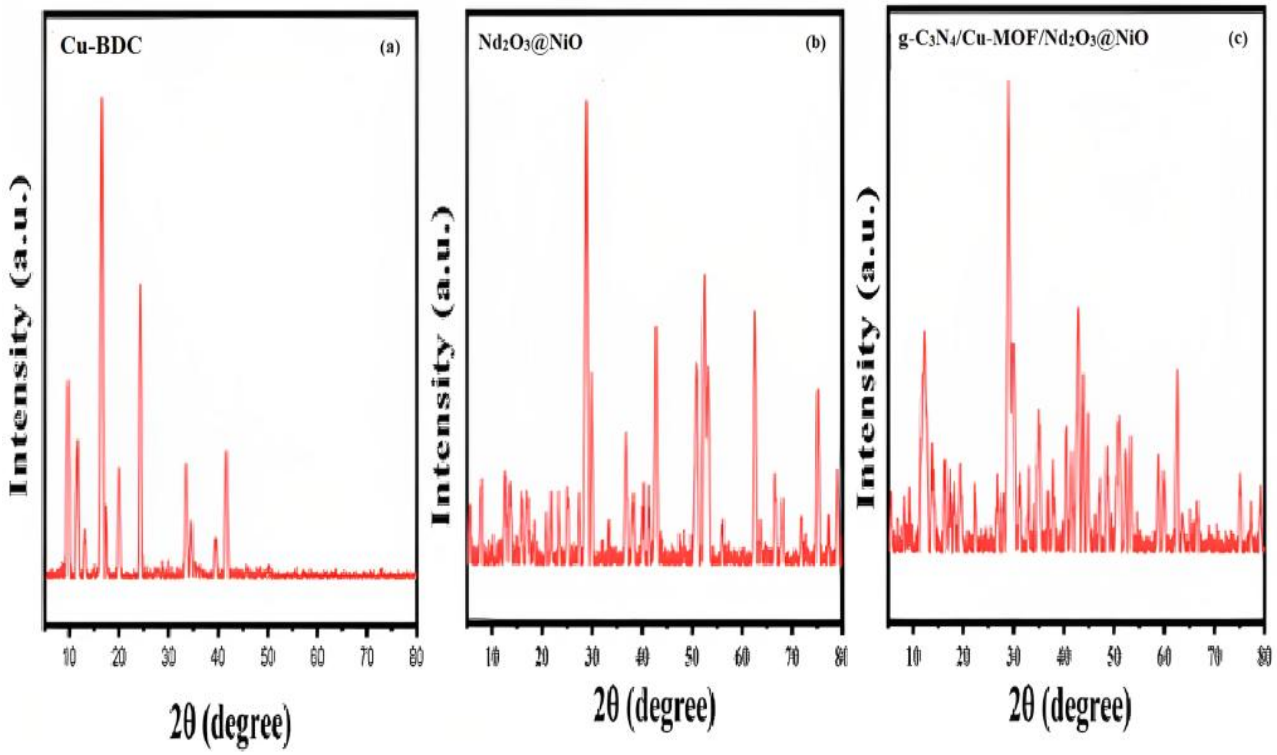


**Figure 5.** X-ray Diffractograms of Cu-BDC MOF (a), $Nd_2O_3$@NiO (b) and g-$C_3N_4$ based Cu-BDC/$Nd_2O_3$@NiO composite

10.57647/ijc.2026.1601.09

### 3.5. Photocatalysis potential evaluation

Photo-catalytic application of the synthesized nanocomposite and its individual components was performed against organic target pollutants, methylene blue (Maximum absorbance ($\lambda_{max}$) for MB ($\lambda_{max}$) was observed at 663 nm. To get optimization of affecting parameters such as pH, conc. of the catalyst, the photo-catalytic activity of the synthesized nanocomposite and its individual components were performed in detail.

#### 3.5.1. *Catalyst Concentration Effect*

The effect of catalyst concentration of nanocomposite and individual components for Methylene blue degradation was examined using 5, 10, 15, and 20 mg concentrations of each catalyst. While the concentration of dye (10 mg/L) was kept constant.

The results are represented in Figure 6. The degradation efficiency using g-$C_3N_4$ was found as 80 %, 66 %, 57 %, 31 % at dose of 5, 10, 15, 20 mg (shown in Figure 6a), using Cu-MOF it was found as 59 %, 50 %, 70 %, 34 % (shown in Figure 6b) and 64 %, 76 %, 81 %, 46 % was observed using $Nd_2O_3$@NiO as photocatalyst (shown in Figure 6c).

The degradation efficiency using the composite was found as 76 %, 90 %, 69 % and 45 %, at catalyst dose of 5, 10, 15, and 20 mg, respectively (shown in Figure 6d). When the amount of catalyst increased, then the surface area or active sites on the photocatalytic surface increased, resulting in the production of more active species or radicals, which leads to efficient photocatalytic degradation.

While at a high concentration, degradation efficiency decreased because at higher catalyst's concentration, the transparency of the solution reduced, the opacity of the suspension increased, which may restrict photon penetration and increase scattering through the surface of the photocatalyst, leading to a decrease in degradation activity [41].

The maximum % degradation efficiency of individual components and the nanocomposite are compared in the form of a graph as shown in Figure 6e.

This graph shows that the nanocomposite shows maximum degradation efficiency as compare to the individual components.

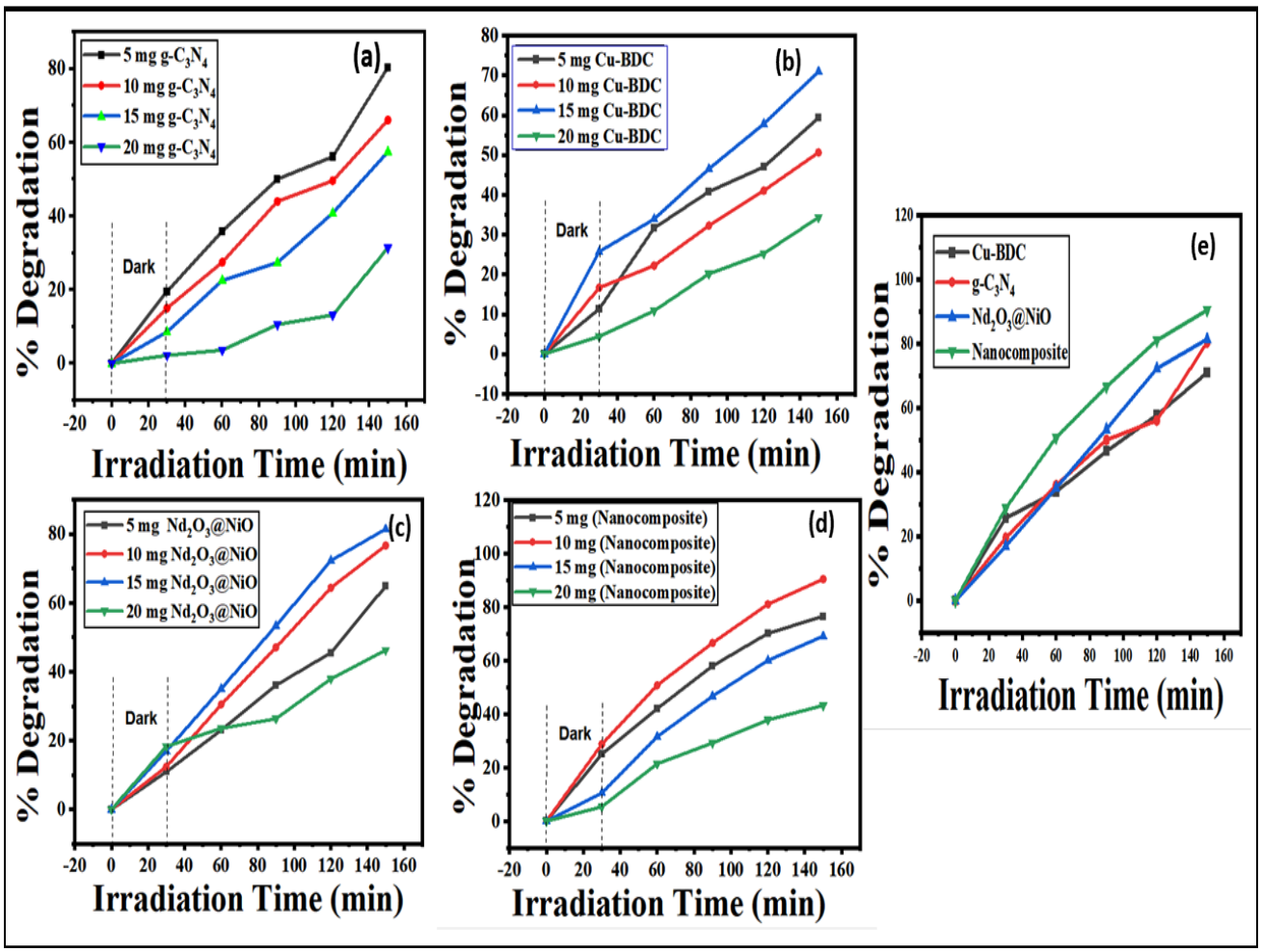


**Figure 6.** (a-d) Photocatalytic degradation percentage vs irradiation time and (e) Overall comparison of maximum % degradation for the composite and its individual components

10.57647/ijc.2026.1601.09

3.5.2. *Effect of various levels of pH on degradation*

The effect of various levels of pH (3-11) on methylene blue degradation using nanocomposite and individual components was examined, and the results are shown in Figure 7. In each experiment, the catalyst dose (10 mg) and dye solution concentration (10 mg/L) were the same, and aqueous NaOH and HCl were used to adjust the dye solution's pH. The degradation efficiency of individual components at pH 3, 5, 9, and 11 was determined as 40, 52, 60, and 75 % for g-$C_3N_4$ (Figure 7a), while Cu-MOF degraded 47, 52 , and 59 %, for methylene blue dye (Figure 7b). The bimetallic oxide composite degraded to 44, 56, 67, and 75 % methylene (Figure 7c). The final composite showed degradation efficiency of 40, 56, 82, and 91%, respectively (Figure 7d) using 3, 5, 7, and 11 pH level. The extreme degradation was attained using pH 11. The composite's photocatalytic activity significantly increased when the pH of the solution rose because of the strong electrostatic interaction between the MB dye (positively charged) and the catalyst's surface (negatively charged) [12, 13]. The optimum pH was obtained by keeping the concentration of the catalyst (10 mg) and dye concentration (10 mg/L) constant. Therefore, finally, optimum conditions of pH 11 and dose of catalyst (10 mg) were obtained for 10 mg/L dye concentration. The surface charge (pHpzc) of the composite was determined using the pH drift method given in Figure 7e. According to the results, the g-$C_3N_4$/Cu-BDC/$Nd_2O_3$@NiO owes a zero-point charge at 5.79 pH. This indicates that the composite surface becomes negatively charged at pH > 5.79 and positively charged at pH < 5.79. It is clear from the experiment's findings that a basic pH environment is better for the adsorption of the cationic dye MB. Because this species has a positive charge at higher pH values, MB dye adsorption is dominant in basic pH solutions. Positively charged compounds and negatively charged catalyst surfaces interact more electrostatically. In a basic environment, this interaction promotes greater adsorption and degradation efficiency. Time on dye' s photodegradation corresponds to the saturation state of the catalyst surface with dye molecules. Photocatalytic degradation would continue to increase until the catalyst surface becomes saturated, i.e., an approximately horizontal line in a degradation vs. time plot represents a stabilization in the photocatalytic degradation rate as shown in Figure S2.

Furthermore, the degradation process was investigated under direct sunlight without a catalyst, but photolysis was negligible, as shown in Figure S3. While in the presence of a catalyst (nanocomposite), efficient degradation was achieved.

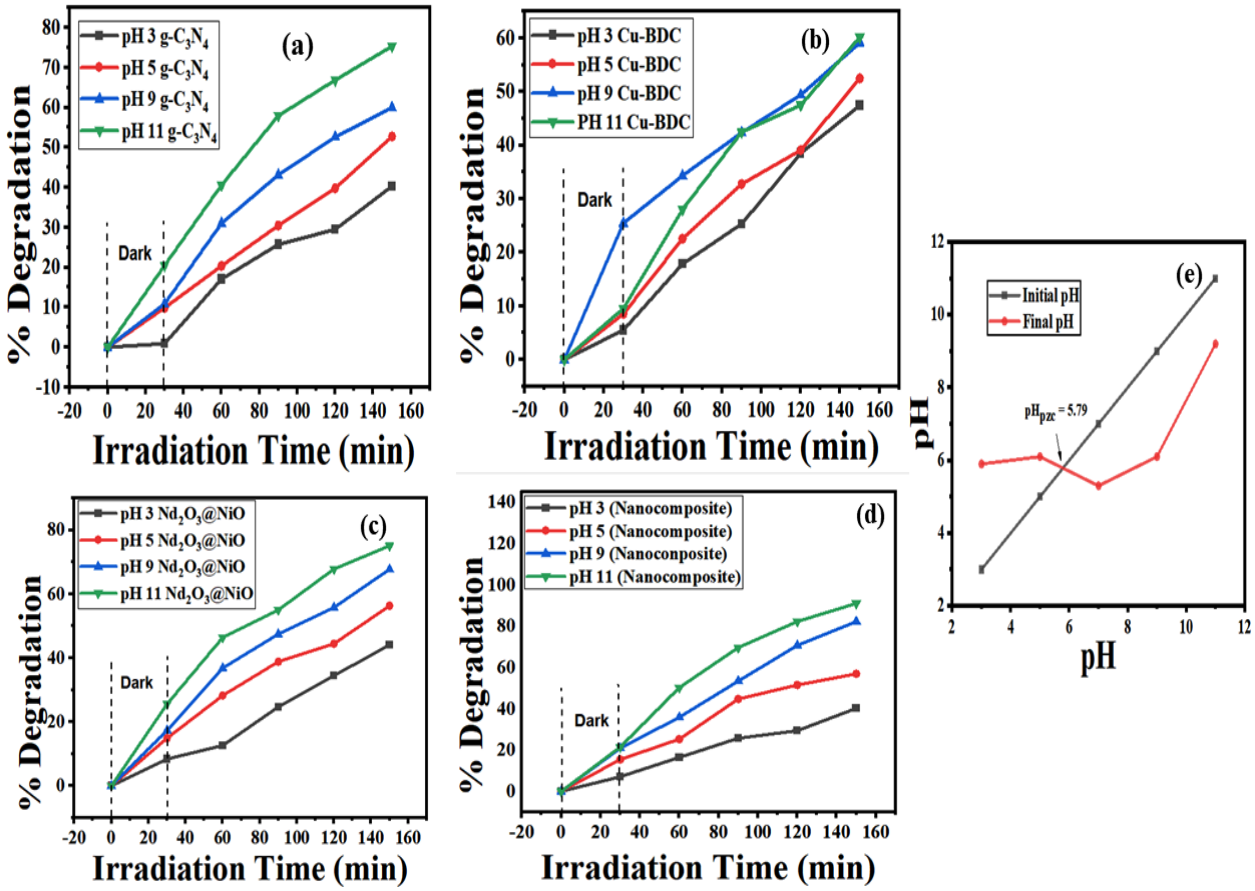


**Figure 7.** (a-c) The photocatalytic degradation vs irradiation time of individual components, (d) composite using various pH levels from 3-11, and (e) Point Charge determination of methylene blue

10.57647/ijc.2026.1601.09

3.5.3. *Adsorption studies*

Each material adsorbed a considerable quantity of dye on its surface according to its adsorption capabilities. The adsorption capacity of constituent components g-$C_3N_4$, Cu BDC, and $Nd_2O_3$@NiO was determined as 75.34 mg/g, 60.2 mg/g, and 75.1 mg/g, respectively.

The maximum adsorption capacity is shown by the composite g-$C_3N_4$/Cu BDC/$Nd_2O_3$@NiO as 91.06 mg/g (Figure S4). Compared to the separate components, this composite structure offers more active adsorption sites and improved dye-catalyst interactions, leading to better dye removal.

### 3.6. Kinetic Study of the degradation reaction

The pseudo-first order kinetic model (equation given below) was applied to investigate the rate of degradation reaction of the composite. The results are indicated in the form of a plot having $\ln(C_o/C_t)$ vs irradiation time as shown in Figure S5. A linear relationship was obtained, which indicates that pseudo-first order has been followed.

$$Kt = \ln\left(\frac{C_o}{Ct}\right) \quad (3)$$

In this equation, K indicates the rate constant. Values of K are calculated from the slope of the graph. The determined rate constant using different concentrations of catalyst and pH level have also been represented in Figure S5(inset). The highest rate constant K value of 0.01791 $min^{-1}$ was obtained in the case of the pH factor, while 0.01662 $min^{-1}$ rate constant K was obtained in the effect of catalyst concentration.

### 3.7. Mechanism of photocalytic degradation

To elucidate the mechanism of photocatalytic degradation, the photocatalyst's band gap is an important parameter that illustrates the possible production of charge carriers (electron and holes).

Generally, the Tauc plot was used to find out the band gaps of individual components and the final composite. The Tauc plot was plotted between $(\alpha h\upsilon)^{1/n}$ on the Y-axis versus $h\upsilon$ on the X-Axis. The Tauc method is based on the relationship between $E_g$ and the optical absorption coefficient ($\alpha$) given below in the form of well known Tauc equation [50].

$$(\alpha h\upsilon)^{1/n} = B(h\upsilon - Eg) \quad (4)$$

where α = absorption coefficient, hυ = energy of the incident photon, B = proportionality constant, Eg = optical band gap and n is power co-efficient which depend upon type of electronic transition which are n = 2 for indirect allowed transition, n = 3 for indirect forbidden transition, n = ½ direct allowed transition, and n = 3/2 direct forbidden transition as mentioned in [51]. Actually, the value of optical band gap (Eg) was calculated by extrapolating a tangent to the curve that was projected to the X-axis, which are given as 2.8 eV (g-$C_3N_4$), 3.3 eV (Cu-MOF), 4.2 eV (bimetallic oxides), and 3.1 eV (composite) (Figure 8A). The reduction of the the band gap in the nanocomposite as compared to Cu-MOF, $Nd_2O_3$@NiO, revealed the efficient combination for photocatalytic degradation.

The schematic mechanism for photocatalytic degradation is given in Figure 8B. By absorbing solar light, photo-catalysts can create electron-hole pairs. This happens when there is enough photon energy in the light to match or exceed the photo-catalyst's band gap energy. The generated electron-hole pairs migrate to the photo-catalyst's surface to take part in a redox reaction. The electrons are pushed to the conduction band. In the meantime, the MB dye is attacked by the holes in the valence band. Furthermore, some of the holes produce hydroxyl radicals when they combine with water, which severely oxidize the methylene blue dye. However, the oxygen is still being attacked by the excited electrons, leading to creation of superoxide anion radicals. These radicals also break down the methylene blue dye, producing carbon dioxide, water, and other less or non-toxic chemicals. Another viable mechanism has been proposed on the basis of distinct band gaps of three components ($Nd_2O_3$@NiO, Cu-MOF, g-$C_3N_4$), which leads to the formation of a heterojunction as shown in Figure 8C. This heterojunction plays an important role in the charge separation of photogenerated electron-hole pairs [26, 29, 52]. Thus, it reduces the charge carrier recombination and maximizes the photodegradation effects. In this proposed mechanism, sunlight hits the surface of $Nd_2O_3$@NiO, and $e^-/h^+$ are generated in CB and VB, respectively. These generated $e^-$ (electrons) are migrated from the CB of $Nd_2O_3$@NiO to the CB of Cu-MOF and finally accumulated at the surface of g-$C_3N_4$ and then react with atmospheric $O_2$ to produce superoxide radicals ($\bullet O_2^-$) through the process of reduction. While the holes (h+) are migrated from the valence band of g-$C_3N_4$ to MOF and $Nd_2O_3$@NiO and react with water or hydroxide to form •OH radicals. These $\bullet O_2^-$ and •OH radicals are then used to degrade the MB dye and produce $CO_2$ and $H_2O$.The reactions (Eq. 5-12) are given below.

### 3.8. Scavenger test

In order to find out the active species responsible for the degradation of the dye, a scavenger test was performed. Generally, it has been observed that hydroxyl radical (•OH), holes ($h^+$), superoxide radicals ($\bullet O_2^-$), and electrons ($e^-$) are the most common active species in the degradation process [12, 13].

$g\text{-}C_3N_4/Cu\text{-}BDC/Nd_2O_3@NiO + h\nu \longrightarrow g\text{-}C_3N_4/Cu\text{-}BDC/Nd_2O_3@NiO\ (e^-_{CB} + h^+_{VB})$ (5)

$g\text{-}C_3N_4/Cu\text{-}BDC/Nd_2O_3@NiO\ (e^-_{CB})\ \text{trapping sites} + O_2 \longrightarrow \bullet O_2^-$ (6)

$\bullet O_2^- + H_2O \longrightarrow \bullet OH_2 + \bullet OH$ (7)

$\bullet OH_2 + H_2O \longrightarrow \bullet OH + H_2O_2$ (8)

$H_2O_2 \longrightarrow 2\bullet OH$ (9)

$g\text{-}C_3N_4/Cu\text{-}BDC/Nd_2O_3@NiO\ (h^+_{VB}) + H_2O \longrightarrow \bullet OH$ (10)

$g\text{-}C_3N_4/Cu\text{-}BDC/Nd_2O_3@NiO\ (h^+_{VB}) + MB \longrightarrow CO_2 + H_2O$ (11)

$\bullet O_2^-$ or $\bullet OH + MB \longrightarrow CO_2 + H_2O$ (12)

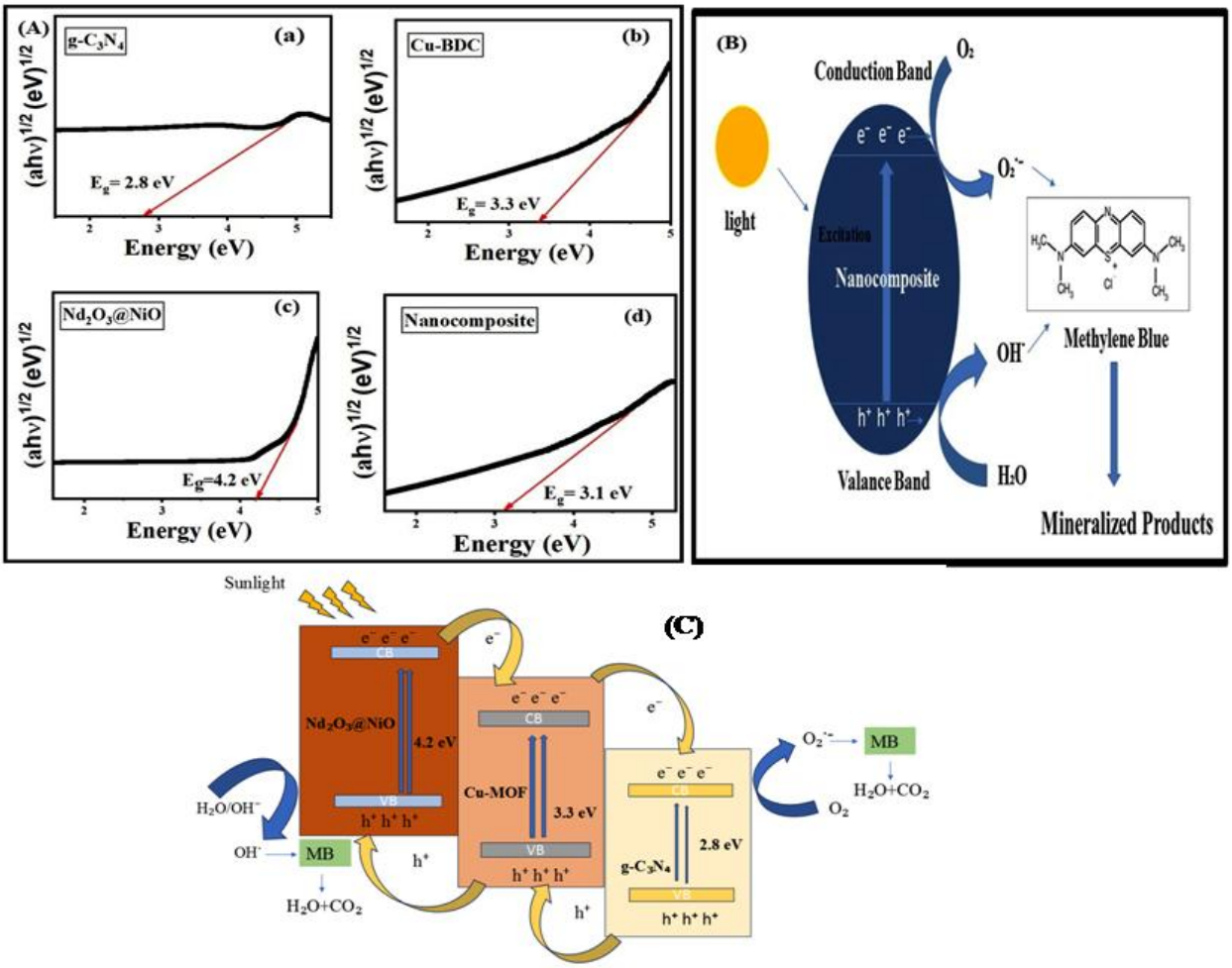


**Figure 8.** Schematic Representation of Photocatalytic Degradation of Methylene Blue and Tauc plots of individual components (a-c) and final composite (d)

Therefore, the mostly used scavengers such as dimethyl sulfoxide (DMSO), sodium ethylenediaminetetraacetate (EDTA-Na), ascorbic acid (ASC), and silver nitrate ($AgNO_3$) have been employed to determine the role of these active species in the degradation of dye.The behavior of other interfering species, such as chloride, iodide, sulphite, sulphate, dichromate, etc can be explored because there is a gap present between understanding the role of scavengers and interfering species. However, the scavengers have been extensively used to determine the mechanism of the degradation process. Figure 9 (a and b) shows the scavenger experiment results, which were conducted to observe the degradation process of methylene blue dye in the existence of the composite $g\text{-}C_3N_4/Cu\text{-}BDC/Nd_2O_3@NiO$. The different scavengers such as dimethyl sulphoxide (DMSO), sodium ethylenediaminetetraacetate (EDTA-Na), ascorbic acid (ASC), and silver nitrate (AgNO3) were used for scavenging hydroxyl radical (•OH) , hole ($h^+$), superoxide radical ($\bullet O_2^-$) and electron (e-), respectively.

The introduction of these scavengers significantly inhibited MB degradation, reducing the efficiency from 91% (without scavengers) to 42% with ASC, 54% with DMSO, 69% with $AgNO_3$, and 80% with EDTA-Na. The sharp decline in removal efficiency is due to the

10.57647/ijc.2026.1601.09

scavenging or quenching effect of scavengers, which react sharply with the reactive species [53].

The stronger quenching effects observed with ASC and DMSO indicate that $\bullet O_2^-$ and •OH radicals are the primary reactive species driving the photodegradation process [16].

### 3.9. Catalyst Reusability

The reusability of the g-$C_3N_4$/Cu-BDC/$Nd_2O_3$@NiO composite was determined in three degradation cycles. In each cycle, an experiment of degradation was conducted for 150 minutes using 100 mL of dye solution under sunlight. At a certain interval, a 5 mL sample was taken, and degradation percentage was measured using a UV-vis spectrophotometer. The catalyst was filtered, washed, and dried each time properly for further use.

The decrease in percentage efficiency of the composite was observed as shown in Figure 9c, which may be due to blockage of active sites after each use. However, a sufficient percentage degradation in the third cycle indicates stability of the composite. According to the findings, the composite can be employed as a photocatalyst for multiple times.

### 3.10. Comparison of photocatalytic degradation with early reported catalysts

The present work has been compared and discussed with some earlier reports. The comparison data is given in Table 1.

Rasheed et al. [4] utilized TA@ZIF-67 nanocomposite as photocatalyst and degrade MB with degradation efficiency of 85 % in 50 min of light irradiation. Ashok et al. [54] reported g-$C_3N_4$/CdS/rGO for the degradation of MB, and obtained a a degradation efficiency was 88.3 % in 80 min.

Tehubijuluw et al. [55] reported synthesis of Zinc Oxide/Zeolite nanocomposite which degrade 76 % of MB in 60 min. Fe(15)/Ni(5)@ZIF-8 composite [3] was used for MB dye degradation with 95.06 % efficiency, but given this efficiency in 180 min, the current work (g-$C_3N_4$/Cu-BDC/$Nd_2O_3$@NiO) shows 91 % degradation in 150 min.

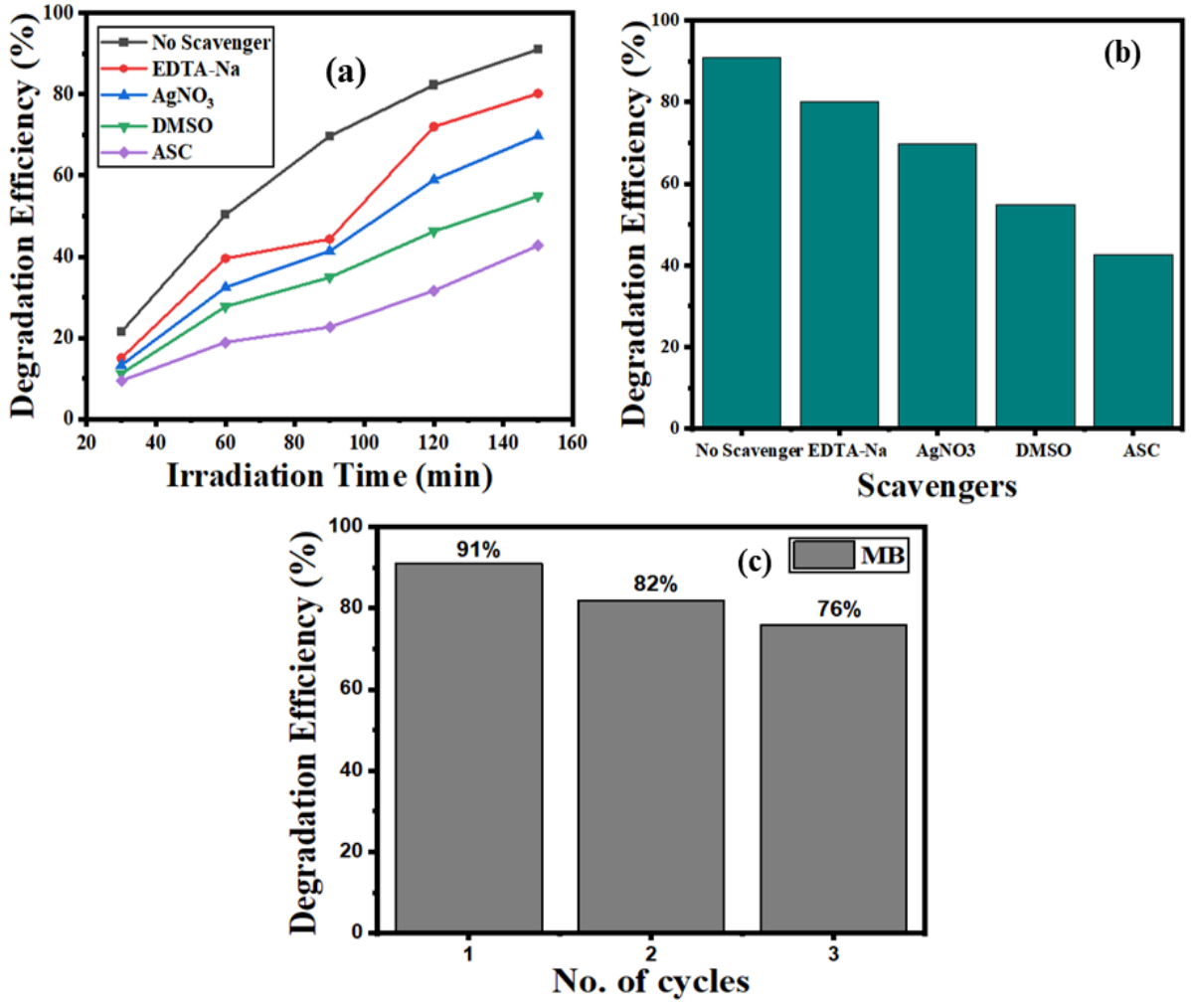


**Figure 9.** Scavenger test (a) line spectra, (b) bar chart using g-$C_3N_4$/Cu-BDC/$Nd_2O_3$@NiO, (c) Reusability test of g-$C_3N_4$/Cu-BDC/$Nd_2O_3$@NiO composite

10.57647/ijc.2026.1601.09

**Table 1.** Comparison of degradation efficiency of some previously reported composites

| Nanocomposite | Pollutant | Pollutant concen. | Catalyst Dosage | Irradiation Time | Efficiency | References |
|---|---|---|---|---|---|---|
| TA@ZIF-67 | MB | 50 mL | 50 mg | 60 min | 85 % | [4] |
| g-$C_3N_4$/CdS/rGO | MB | 100 mL | 0.5 g $L^{-1}$ | 80 min | 88.3% | [54] |
| Zinc Oxide /Zeolite | MB | 100 mg $L^{-1}$ | 34 % w/w | 60 min | 76% | [55] |
| Fe(15)/Ni(5)@ZIF-8 | MB | 10 mL | 10 mg | 180 min | 95.06 % | [3] |
| g-$C_3N_4$/Cu-BDC/$Nd_2O_3$@NiO | MB | 10 PPM | 10 mg | 150 min | 91% | This Work |

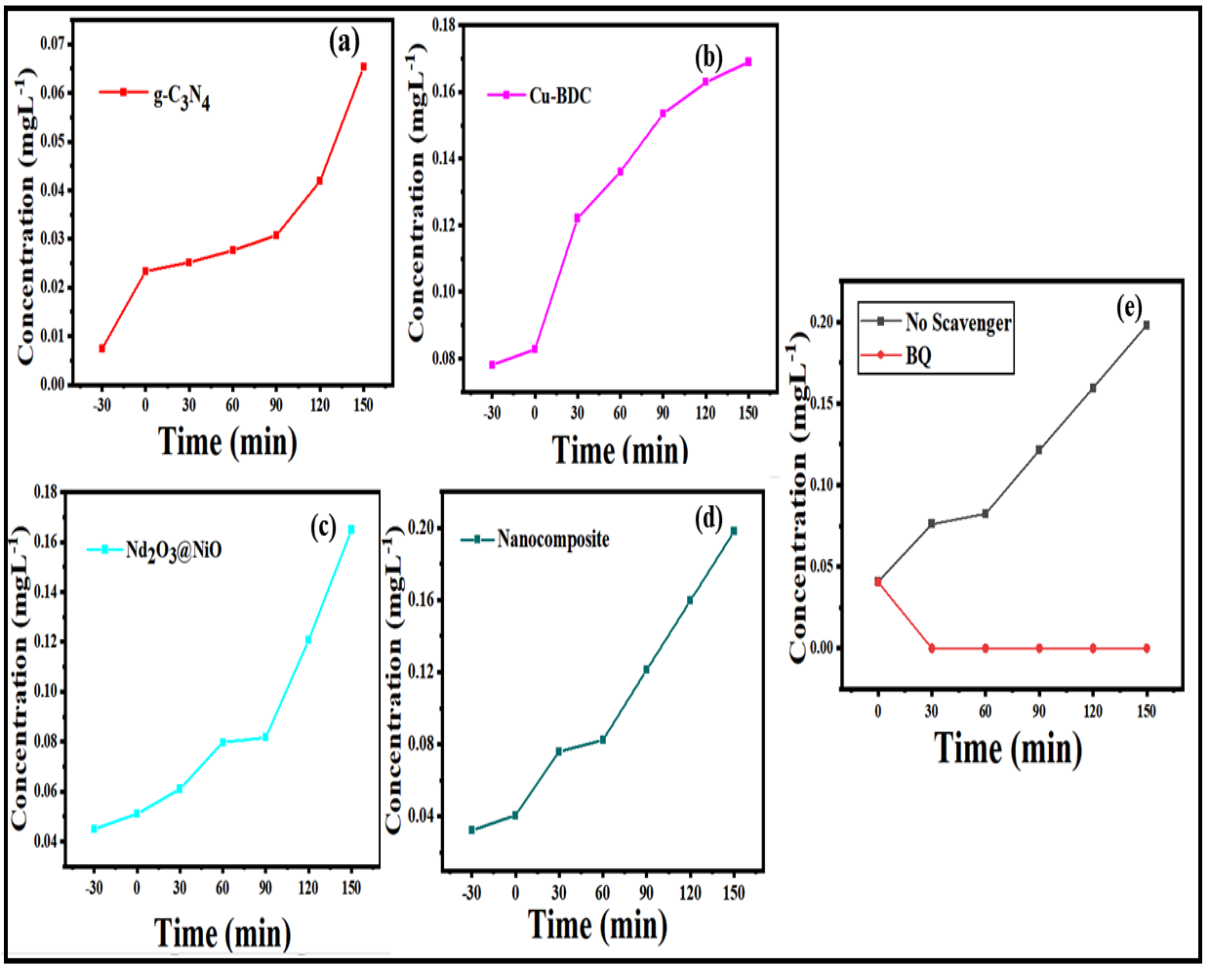


**Figure 10.** (a-c) Photocatalytic hydrogen production using individual components, (d) composite, and (e) Scavenger test for $H_2O_2$

### 3.11. $H_2O_2$ Production

The photocatalytic hydrogen peroxide production was also tested using composite and its individual components. The results are represented in Figure 10. The concentration of $H_2O_2$ was measured at 350 nm using UV-Vis spectrophotometer.

The concentration of $H_2O_2$ was increased with time as indicated in Figure 10. The nanocomposite g-$C_3N_4$/Cu-BDC/$Nd_2O_3$@NiO showed more $H_2O_2$ production at a rate of 0.19 mg/L, than the individual components as represented in Figure 10. It has been recognized that there are two reaction paths for photocatalytic $H_2O_2$ production: the single-electron reduction route and the two-electron reduction route.Single-electron reduction is shown in equation '1−4', while equation '5' is the two-electron reduction route.

$$O2+e- \rightarrow .O2- \quad (13)$$

$$O2- + H+ \rightarrow HO2. \quad (14)$$

$$HO2. + e- \rightarrow HO2- \quad (15)$$

$$HO2- + H+ \rightarrow H2O2 \quad (16)$$

$$O2 + 2H+ + 2e- \rightarrow H2O2 \quad (17)$$

For elucidating the $H_2O_2$ production method, the $^{\bullet}O_2^-$ scavenger Benzoquinone (BQ) was employed (Figure 10 (e)). In the existence of BQ, $H_2O_2$ production is negligible in contrast to without BQ. So, it can be concluded that BQ utilizes all the $^{\bullet}O_2^-$ and inhibits $H_2O_2$ production, suggesting that $^{\bullet}O_2^-$ is a vital intermediate in the reduction

pathway. Based on this result, it is assumed that $H_2O_2$ production is by the single-electron path.

## 4. Conclusion

In the current study, a novel composite was successfully synthesized by the ultrasound assisted wet impregnation method and comprehensively characterized by FTIR, XRD, SEM, and EDX analysis. The vibrational bands, morphological characteristics, crystalline nature, and elemental composition were conferred successfully. The respective metal-oxygen vibrational bands were observed in the infrared spectrum of the composite and well compared with the infrared spectra of individual components. The crystalline nature of the composite and its individual components was observed in XRD analysis. Flake-like morphology of g-$C_3N_4$/Cu-BDC/$Nd_2O_3$@NiO was observed in Scanning electron microscopy (SEM) images. The elemental analysis of the composite and its individual components was confirmed by EDX analysis. The photocatalytic degradation of methylene blue (MB) dye was successfully done under sunlight irradiation. Various operating parameters, such as concentrations of catalyst and pH levels (acidic and basic), were optimized. The maximum degradation was 91% at pH 11 and a 10 mg catalyst dose. The photocatalytic production of hydrogen peroxide was achieved at a production rate of 0.19 mg/L using g-$C_3N_4$/Cu-BDC/$Nd_2O_3$@NiO nanocomposite. The dual photocatalytic applications of -$C_3N_4$/Cu-BDC/$Nd_2O_3$@NiO nanocomposite indicated its excellent potential as a photocatalyst.

**Author's Contribution**
All Authors have contributed equally to prepare the paper.

**Conflict of interest**
The authors declare that they have no known competing financial interests or personal relationships that could have appeared to influence the work reported in this paper.

**Data availability statement**
All the data relevant to this research project have been included in the manuscript.

## References


[1] P. Intaphong, P. Inphak, S. Tandorn, K. Chokethawai, C. Randorn, Iran. J. Catal. **15** (2025) 1-16. https://doi.org/10.57647/j.ijc.2025.503.28

[2] H. M. Elmehdi, B. Malathi, S. Begum, Surf. Interfaces. **78** (2025) 108106. https://doi.org/10.1016/j.surfin.2025.108106

[3] S. Saenab, O. P. Arjasa, F. I. Pambudi, D. Siswanta, RSC Adv. **15** (2025) 44893-44908. https://doi.org/10.1039/D5RA05662D

[4] S. Rasheed, S. A. Khan, M. A. Nazir, S. Ali, M. Younas, R. Iqbal, M. Mansha, M. K. Tufail, M. Arshad, A. Rehman, Chemistry Select. **9** (2024) 1-10. https://doi.org/10.1002/slct.202403807

[5] A. Mehrehjedy, P. Kumar, Z. Ahmad, P. Jankoski, A. S. Kshirsagar, J. D. Azoulay, X. He, M. K.Gangishetty, T. D.Clemons, X. Gu, W. Miao, S. Guo, ACSO mega. **9** (2024) 49239-49248. https://doi.org/10.1021/acsomega.4c06142

[6] N. F. T. Siddiqui, F. Mushtaq, J. Mahar, M. Tariq, S. Haider, K. Alam, A. Iqbal, Int. J. Mater. Res. **116** (2025) 287-302 . https://doi.org/10.1515/ijmr-2024-0138

[7] S. Tibebu, M. A. Gnaro, A. M. Kebede, A. A. Ammona, T. Sime, S. Ayalneh, M. A. Feyisa, M. Jabli, Results Eng. **28** (2025) 108143. https://doi.org/10.1016/j.rineng.2025.108143

[8] P. Eswaran, P. D. Madasamy, K. Pillay, H. Brink, Biomass Convers. Biorefinery. **15** (2025) 12347-12367. https://doi.org/10.1007/s13399-024-05999-z

[9] P. Laokul, and N. Kanjana, *Colloids Surf. A: Physicochem.* **731** (2025) 139034 https://doi.org/10.1016/j.colsurfa.2025.139034

[10] S. Das, S. V. Chituru, S. K.Panigrahi, S. B. Bhutt, and S. Majumdar, Sep. Purif. Technol. **383** (2025) 136142. https://doi.org/10.1016/j.seppur.2025.136142

[11] RM. Ahmaruzzaman, S. R. Mishra, Mater. Res .Bull. **143** (2021) 111417. https://doi.org/10.1016/j.materresbull.2021.111417

[12] S. Ghazanfar, K. H. Shah, H. M. Asif, M. Sirajuddin, S. Hussain, M. Tariq, Int. J. Environ. Anal. Chem. **105** (2025) 2344-2368. https://doi.org/ 10.1080/03067319.2024.2313660

[13] K. S. Ali, K. H. Shah, H. M. Asif, M. A. Khan, S. Hussain, M. Tariq, Int. J. Environ. Res.**66** (2024) 1-19. https://doi.org/10.1007/s41742-024-00617-2

[14] G. Subhrajyoti, Abhijeet Rana, Shyam Biswas, Chem. Mater. **36** (2024) 99-131. https://doi.org/10.1021/acs.chemmater.3c02459

[15] S. Zhou, L. Lu, D. Liu, J. Wang, H. Sakiyama, M. Muddassir, A. Nezamzadeh-Ejhieh, J. Liu, Cryst Eng Comm **23** (2021) 8043-8052. https://doi.org/10.1039/D1CE01264A

[16] L. Song, Y. Yang, M. Zhang, J. Yan, H. Xia, L. Cui, Int. J. Biol Macromol. **333** (2025) 148964. https://doi.org/10.1016/j.ijbiomac.2025.148964

[17] J. Sahadevan, V. Siva, A. Murugan, A. S. Shameem, M. Pannerselvam, M. Arunpandian, T. H. Oh, J.Alloys Compds. **1050** (2025) 185414. https://doi.org/10.1016/j.jallcom.2025.185414

[18] A. R. Bagheri, M. Ghaedi, Arab. J. Chem. **13** (2020) 5218-5228. https://doi.org/10.1016/j.arabjc.2020.02.020

[19] V. D. Doan, T. L. Do, T. M. T. Ho, V. T. Le, H. T. Nguyen, Sep. Sci. Technol. **55** (2020) 444-455. https://doi.org/10.1080/01496395.2019.157726

[20] B. Abdollahi, S. Farshnama, E. A. Asl, A. Najafidoust, M. Sarani, Inorg. Chem. Commun.**138** (2022) 109236. https://doi.org/org/10.1016/j.inoche.2022.109236

[21] Y. Wang, M. Ding, Z. Li,M. Li, Surf. Interfaces. **44** (2024) 103585. https://doi.org/10.1016/j.surfin.2023.103585

[22] A. Kumar, A. M. Hussein, F. M. Altalbawy, M. Kaur, H. Kaur, S. S. Jalal, S. H. Z. Al-Abdeen, K. Muzammil, M. Alhadrawi, Arab. J. Chem. **17** (2024) 105912. https://doi.org/org/10.1016/j.arabjc.2024.105912

[23] G. Xin, Y. Meng, J. Chem. **2013** (2013) 1-5. https://doi.org/org/10.1155/2013/187912

[24] Y. Zhang, J. Lu, M. R. Hoffmann, Q. Wang, Y. Cong, Q. Wang, H. Jin, RSC Adv. **5** (2015) 48983-48991. https://doi.org/10.1039/C5RA02750Ks

[25] J. M. Yassin, A. M. Taddesse, M. Sánchez-Sánchez, Catal. Today. **390** (2022) 162-175. https://doi.org/org/10.1016/j.cattod.2021.11.037

[26] R. Sheikhsamany, A. Nezamzadeh-Ejhieh, J. Mol. Liq. **430** (2025) 127829. https://doi.org/10.1016/j.molliq.2025.127829

[27] S. Sharafzadeh, J. Zolgharnein, A. Nezamzadeh–Ejhieh, S. D. Farahani, Surf. Interfaces. **59** (2025) 105917. https://doi.org/10.1016/j.surfin.2025.105917

[28] S. Sharafzadeh, A. Nezamzadeh–Ejhieh, J. Zolgharnein,Chem. Phys. Impact. **11** (2025) 100963. https://doi.org/10.1016/j.chphi.2025.100963

[29] A. Yousefi, A. Nezamzadeh-Ejhieh, Iran. J. Catal. **11** (2021) 247-259. https://doi.org/oiccpress.com/ijc/article/view/3600

[30] M. Raza, N. F. T. Siddiqui, M. Tariq, K. Mahmood, S. Hussain, Int. J. Environ. Anal. Chem. (2025) 1-26. https://doi.org/10.1080/03067319.2025.2584474

[31] G. Liu, M. Mamat, Y. Baikeli, X. Dong, Heliyon. **10** (2024) e29894. https://doi.org/10.1016/j.heliyon.2024.e29894

[32] A. B. Siddique, M. A. Shaheen, S. Shafeeq, A. Abbas, Y. Zaman, M. Z. Ishaque, M. Aslam, Adv. Mater. **6** (2025) 1330-1344. https://doi.org/10.1039/D4MA01078G

[33] S. Minisha, J. Johnson, S. M. Wabaidur, J. K. Gupta, S. Aftab, M. R. Siddiqui, W. Lai. Sustainability. **15** (2023) 14552. https://doi.org/org/10.3390/su151914552

[34] A. Akbari, Z. Sabouri, H. A. Hosseini, A. Hashemzadeh, M. Khatami, M. Darroudi, Inorg. Chem. Commun. **115** (2020) 107867. https://doi.org/10.1016/j.inoche.2020.107867

[35] S. Legmairi, S. Meneceur, A. Bouafia, S. E. Laouini, S. A. Alshareef, K. A. Essa, H. A. Almukhlifi, M. L. Tedjani, Farid Menaa, Biomass Convers. Biorefinery. **14** (2024) 18469-18479. https://doi.org/org/10.1016/j.jece.2020.104725

[36] E. Arulkumar, S. Thanikaikarasan, Optik. 302 (2024) 171685. https://doi.org/10.1016/j.ijleo.2024.171685

[37] Y. Tang, J. Qiu, D. Dai, G. Xia, B. Fang, Y. Li, J. Yao, Sep. Purif. Technol. **354** (2025) 129350. https://doi.org/10.1016/j.seppur.2024.129350

[38] H. Xie, Y. Zheng, X. Guo, Y. Liu, Z. Zhang, J. Zhao, W. Zhang, Y. Wang, Y. Huang, ACS Sustain. Chem. Eng. **9** (2021) 6788-6798. https://doi.org/10.1021/acssuschemeng.1c01012

[39] J. Y. Yue, L. P. Song, Y. F. Fan, Z. X. Pan, P. Yang, Y. Ma, Q. Xu, B. Tang, Angew. Chem. Int. Ed **62** (2023) 09624. https://doi.org/10.1002/anie.202309624

[40] M. M. Rahman, A. Wahid, A. M. Asiri, New J. Chem. **43**(2019) 17395-17402. https://doi.org/10.1039/C9NJ05050G

[41] A. Khurshid, K. Shah, H. Asif, M. Khan, A. Hussain, M. Tariq, Int. J. Environ.Sci. Technol. **182** (2025) 1-18. https://doi.org/10.1016/j.apcatb.2015.09.029

[42] Q. Zhang, S. Fu, H. Li, Y. Liu, Bio Resources. **8** (2013) 3699-3705.

[43] M. Zeeshan, S. Ghazanfar, M. Tariq, H. M. Asif, A. Hussain, M. Usman, M. A. Khan, K. Mahmood, M. Sirajuddin, M. Imran, Renew. Energy, **210** (2023) 800-809. https://doi.org/10.1016/j.renene.2023.04.077

[44] A. Chauhan, A. A. P. Khan, A. Sudhaik, R. Kumar, K. P. Katin, S. Kaya, P. Raizada, P. Singh, N. Azum, K. A. Alzahrani, J. Sol-Gel Sci. Technol, **112**(2024) 688-702. https://doi.org/10.1007/s10971-024-06556-w

[45] R. C. Dante, P. M. Ramos, A. Correa-Guimaraes, J. Martín-Gil, Mater. Chem. Phys **130** (2011) 1094-1102. https://doi.org/10.1016/j.matchemphys.2011.08.041

[46] S. A. Al-Harbi, Y. Q. Almulaiky, Heliyon. **10** (2024) 28396. https://doi.org/org/10.1016/j.heliyon.2024.e28396

[47] M. Arunpandian, K. Selvakumar, A. Raja, P. Rajasekaran, M. Thiruppathi, E.R. Nagarajan, S. Arunachalam, Colloids Surf. A: Physicochem. Eng. Asp. **567** (2019) 213-227. https://doi.org/10.1016/j.colsurfa.2019.01.058

[48] A. Saleem, A. Iqbal, U. Younas, A. Ashraf, S. H. Al-Mijalli, F. Ali, M. Pervaiz, Z. Saeed, A. Nazir, M. Iqbal, Arab. J. Chem. **17** (2024) 105545. https://doi.org/10.1016/j.arabjc.2023.105545

[49] I. W. Sutapa, B. V. Palapessya, F. A. Souhoka, A. Bandjar, Trends Sci. **21** (2024) 7163-7163. https://doi.org/10.48048/tis.2023.7163

[50] J. Tauc, R. Grigorovici, A. Vancu, Phys. Status Solidi, **15** (1966) 627–637. https://doi.org/10.1002/pssb.19660150224

[51] A. Escobedo-Morales, I. I. Ruiz-Lopez, M. Ruiz-Peralta, L. Tepech-Carrillo, M. Sanchez- Cantu, J. E. Moreno-Orea, Heliyon **5** (2019) 01505. https://doi.org/org/10.1016/j.heliyon.2019.e01505

[52] M. Z. Ishaque, Y. Zaman, A. Arif, A. B. Siddique, M. Shahzad, D. Ali, M. Faizan, RSC adv. **13** (2023) 30838-30854. https://doi.org/10.1039/D3RA05170F

[53] A. Ahmadian, S. Ahmadi, B. Goharrizi, Int. J. Environ. Sci. Technol. **20** (2023) 6433-6448. https://doi.org/10.1007/s13762-023-04908-7

[54] S. Ashok, N. Kumaresan,H. C. D. Souza, V. Jayalakshmi, T. F.de Oliveira, B.Neppolian, V. Ganesh, Surf. Interfaces. **73** (2025) 107474. https://doi.org/org/10.1016/j.surfin.2025.107474

[55] H. Tehubijuluw, R. Subagyo, Y. Kusumawati, D. Prasetyoko, Sustain. Environ. Res.**32** (2022) 1-12. https://doi.org/10.1186/s42834-021-00113-8